

Transformation Superplasticity of Zirconium

PETER ZWIGL and DAVID C. DUNAND

A tensile strain of 270 pct was achieved for coarse-grained zirconium subjected to transformation superplasticity conditions, where strain increments are accumulated upon repeated thermal cycling around the allotropic transformation temperature under the biasing effect of a uniaxial tensile stress. The strain increment per cycle was found to consist of two equal contributions from transformations on heating and cooling and to increase linearly with the applied stress. The measured strain increments are in good quantitative agreement with predictions based on the average internal stress during the transformation, which was determined independently from experimental transformation times. As the cycling frequency is raised, the average strain rate increases (a maximum value of $1.3 \cdot 10^{-4} \text{ s}^{-1}$ was measured), but the strain increment per cycle decreases above a critical cycling frequency, for which the sample gage section undergoes only a partial phase transformation. The resulting reduction in internal mismatch and increase in internal stress are modeled using the experimental observation that β -Zr deforms by a mixture of diffusional and dislocation creep in the stress range of interest.

I. INTRODUCTION

Superplastic deformation is characterized phenomenologically by tensile failure strains above 100 pct and can be classified into two mechanism types: fine-structure superplasticity and internal-stress superplasticity.^[1] The former type of superplasticity relies on grain-boundary sliding and is operative in metals with grains smaller than 10 μm , which must be stable at the temperature of deformation. This can be achieved through duplex microstructures or through grain-boundary pinning by fine second-phase particles.^[1] Since pure metals display neither duplex structures nor grain-boundary pinning, they exhibit rapid grain growth at elevated temperatures and are, thus, typically incapable of fine-structure superplasticity. However, certain pure metals can deform superplastically by the second mechanism (internal-stress superplasticity), where internal mismatch stresses are biased by an external stress, resulting in a strain increment. These mismatch stresses and the resulting strain increments can be repeatedly produced by thermal cycling of pure metals exhibiting coefficients of thermal expansion anisotropy^[1,2] (e.g., Zn,^[3,4,5] and U^[3,4,6]) and/or an allotropic phase transformation^[1,7] (e.g., Fe,^[8,9,10] Co,^[8,11] Ti,^[8,12] Zr,^[8,13] and U^[8]). Since the only requirement for internal-stress superplasticity is the repeated creation of internal mismatch stresses, these pure metals can be deformed superplastically by this alternate mechanism independently of their grain size.

In transformation superplasticity, internal mismatch stresses are produced by the volumetric difference between the two allotropic phases $|\Delta V/V|$ (referred to as $\Delta V/V$ in this article). A net plastic strain increment is produced in the direction of the applied stress after each phase transformation as a result of the accommodation of these internal

mismatch stresses by the weaker allotropic phase, which can deform either by time-independent plastic yield or by a time-dependent creep mechanism such as dislocation creep or diffusional creep. Transformation superplasticity was systematically investigated first by Greenwood and Johnson,^[8] who developed a model predicting a linear relationship between the applied stress (σ) and the plastic strain increment per transformation ($\Delta\epsilon$),

$$\Delta\epsilon \approx \frac{2}{3} \cdot \frac{\Delta V}{V} \cdot \frac{\sigma}{\sigma_0} \cdot \frac{5 \cdot n}{(4 \cdot n + 1)} \quad [1]$$

where σ_0 is the average internal stress (averaged over both transformation time and spatial orientation of the phase transformation) of the plastically deforming weaker phase, and n is the stress exponent of the creep law describing the plastic accommodation. Greenwood and Johnson^[8] also considered the case of ideal plastic yielding at low homologous temperatures, which can be described with Eq. [1] by replacing σ_0 by the yield stress (σ_y) of the weaker phase and by letting n tend to infinity.

Equation [1], which is only valid for small applied stresses, was later extended analytically^{14,15} to high applied stresses, where a nonlinear stress-strain behavior is predicted for plastically yielding materials (e.g., Fe, Co, and $U_{\alpha/\beta}$). Similarly, Mitter¹⁶ gives a numerical solutions for the nonlinear case of high applied stresses for materials deforming by yield and by creep (e.g., Ti, Zr, and $U_{\beta/\gamma}$).

As seen from Eq. [1], low values for the yield stress or the internal stress result in large strain increments. Thus, phase transformations occurring at high homologous temperatures, where the material is weak, are most suitable for deformation by transformation superplasticity. However, high cycling temperatures also promote creep outside the transformation range, so that experimentally measured plastic strain accumulated after a full cycle often includes appreciable amounts of creep strain unrelated to the superplastic strain increment. Creep is furthermore undesirable, because it promotes cavitation and neck instability, which reduce the total strain to failure. Thus, the observation of transformation superplasticity (large elongation to fracture and linear dependence between applied stress and strain increment= ϵ . [1]) depends sensitively on suppressing creep

PETER ZWIGL, formerly Research Assistant, Department of Materials Science and Engineering, Massachusetts Institute of Technology, Cambridge, MA 02139, is Senior Process Engineer, Intel Corp., Santa Clara, CA 95052. DAVID C. DUNAND, Associate Professor, is with the Department of Materials Science and Engineering, Northwestern University, Evanston, IL 60208.

Manuscript submitted December 12, 1997.

outside the transformation range, which can be achieved by optimizing the temperature cycle profile and the sample geometry.

In the present article, we investigate transformation superplasticity in pure zirconium, which was chosen for the following three reasons. First, to our knowledge, only two studies^[8,13] exist on the transformation plasticity of zirconium. Second, these studies did not report values for failure strains, a necessary condition for demonstrating transformation superplasticity. Third, zirconium shows an allotropic phase transformation at $T_{\alpha/\beta} = 863$ °C ($T_{\alpha/\beta}/T_m = 0.53$),^[17] where creep is the dominant deformation mechanism.^[18] Thus, zirconium can be used to test the numerical predictions of Mitter^[16] for a creeping material transforming under high applied stresses. As described previously, this can only be achieved if creep outside the phase transformation range is minimized, a condition we fulfill by modifying the usual geometry for superplastic samples. Furthermore, we use measured thermal characteristics during the phase transformation to calculate the average internal stress, which is compared to predictions from mechanical models.

II. EXPERIMENTAL PROCEDURES

The material used was unalloyed zirconium (Zircadyne 702 from Wah Chang, Albany, OR) with an extra-low oxygen content (Table I). A flat tensile sample was machined with its gage length parallel to the rolling direction. Because the sample heads (length: 28.1 mm, width: 14.0 mm, thickness: 4.44 mm, hole diameter: 5.07 mm) were much larger than its gage section (length: 19.85 mm, width: 5.10 mm, thickness: 4.44 mm), only 12 pct of the total sample volume was in the gage section.

Thermal cycling and isothermal creep experiments were conducted under small uniaxial tensile stresses in a custom-designed apparatus (Figure 1). Rapid heating was achieved by using four symmetrically-arranged radiant heaters, with a total nominal power of 8 kW, concentrated on a focal line 280 mm in length. The temperature was controlled at the sample surface (point A in Figure 1(b) and (c)) and monitored at the head of the sample (point B in Figures 1(b) and (c)) with INCONEL*-shielded, boron-nitride coated,

*INCONEL is a trademark of INCO Alloys International, Inc., Huntington, WV.

grounded K-type thermocouples, with a small diameter of 1.6 mm, to minimize the response time. Both thermocouples were subjected to (1) a radiative heat flux to, and from, the sample surface and the heaters; (2) a conductive heat flux through the sample; and (3) a convective heat flux caused by the inert gas. For isothermal conditions, where these heat fluxes are at steady state, the temperatures measured corresponded to the internal sample temperature. However, under transient conditions, *i.e.*, temperature cycling, the thermocouples measured a combination of surface temperature and surrounding temperature. The thermocouple B, positioned at the sample head, was farther from the focal line of the heaters and, thus, experienced a lower heat flux density than the controlling thermocouple A located at the sample surface.

Square-wave temperature profiles were applied at the

Table I. Sample Chemical Composition (Parts per Million)

	C	H	N	O
As-received	<20	4	<20	340
After thermal cycling	42	150	40	360

sample surface with temperatures at the tip of thermocouple A (T_A) between $T_A = 810$ °C and 940 °C and cycling frequencies (ν) between $\nu = 6$ and 30 h⁻¹. A special feature of the experiments was that only the gage section was fully exposed to the radiative heat flux, whereas the sample heads were largely shielded from the radiation (Figure 1(b)). Alumina pins and spacers (Figure 1(c)), as well as low-conductivity INCONEL pullheads and pullrods, minimized heat transfer through the sample heads, so that sample cooling was mainly controlled by radiation from the surface of the gage section. The sample was surrounded by a quartz tube flushed with purified argon, produced by flowing 99.999 pct pure argon through a titanium powder bed held at a temperature of 1000 °C. The sample stress was adjusted manually by applying weights to the pullrod. The force from the spring bellow (Figure 1(a)) compensated the stress increase due to the sample cross-sectional reduction, so that constant stress conditions were maintained over a defined deformation range.

The deformation, which was measured by a linear-voltage displacement transducer placed at the cold end of the lower pullrod, included the thermal dilatation of the whole load train and, therefore, did not represent the sample deformation under transient temperature conditions. However, the plastic deformation measured under steady-state conditions and over full-temperature-cycle periods was only due to the sample plastic deformation.

The same sample was subjected to both isothermal creep and thermal cycling under stress in an experiment consisting of five successive parts. In the first part, the sample was heated to 810 °C under a low stress (0.3 MPa) until the deformation rate of the load train due to thermal expansion was below the detection limit of the apparatus ($d(\Delta D)/dt < 4$ μm · h⁻¹). Creep was then measured at 810 °C at different stress levels between 0.6 and 2.0 MPa and at 910 °C at a constant stress of 1.0 MPa, allowing enough time to reach steady state at each stress and temperature. In the second part of the experiment, the sample was thermally cycled with a frequency of 10 h⁻¹ between the lower cycling temperature (T_l) as measured by thermocouple A $T_l = 810$ °C, and the upper cycling temperature (T_u), $T_u = 910$ °C, at stresses of 0.3 and 1.0 MPa. Steady-state isothermal creep was established before and after each cycling segment, which consisted of four to eight individual cycles. In the third part of the experiment, cycling segments were conducted where the cycling frequency was varied between 6 and 15 h⁻¹ at a constant stress of 1.0 MPa and with temperature amplitudes of $T_l = 810$ °C and $T_u = 910$ °C. These cycling segments were also preceded and succeeded by isothermal creep measurements at the upper cycling temperature. The fourth and fifth parts of the experiment consisted of a series of stress variations at frequencies of $\nu = 15$ and 30 h⁻¹, respectively, with $T_l = 810$ °C and $T_u = 910$ °C to 940 °C. The stress was changed in discrete steps during the thermal cycling, with eight to twenty cycles measured at each stress level. The experiment was stopped after 25

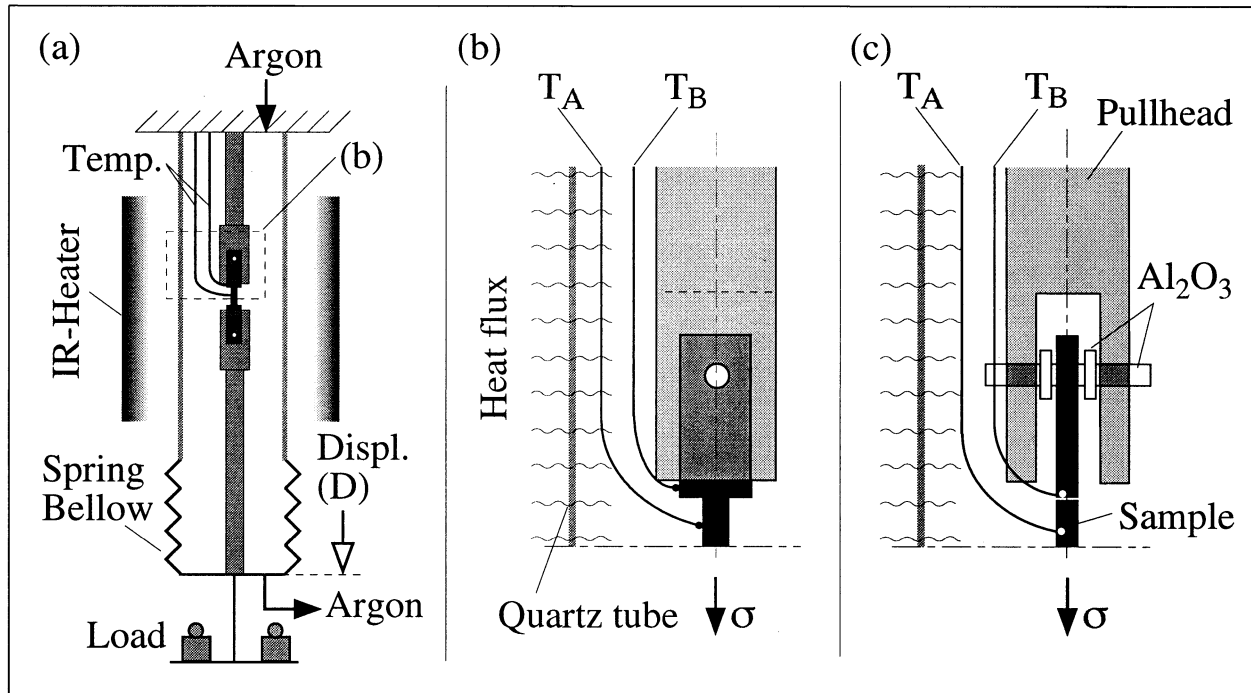


Fig. 1—(a) Schematic of the experimental setup. (b) and (c) Two detailed orthogonal views.

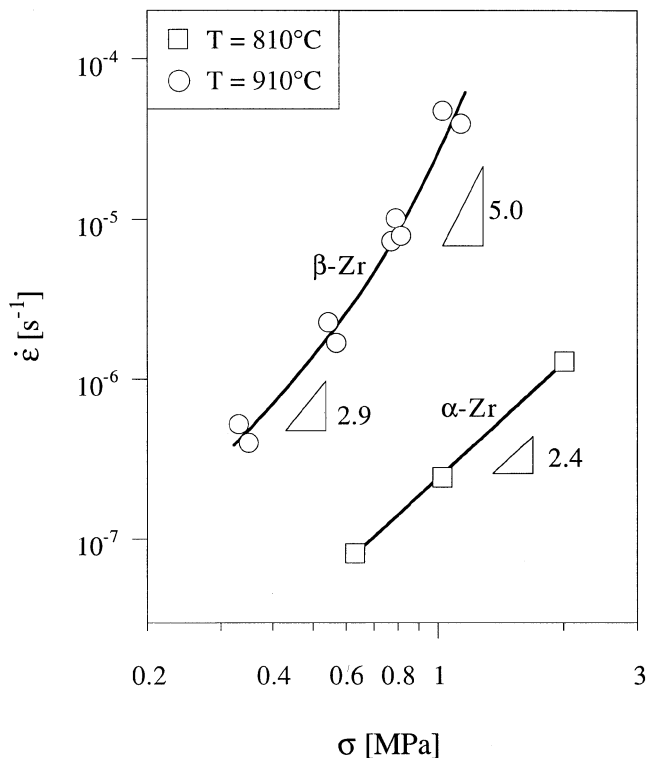


Fig. 2—Isothermal creep rate as a function of the applied stress for α -Zr at 810 °C and β -Zr at 910 °C.

hours and a total of 212 cycles, because the travel limit of the apparatus had been reached.

III. RESULTS

Figure 2 shows the isothermal steady-state creep rate of α -Zr at 810 °C and β -Zr at 910 °C, as measured during the

first and second part of the experiment. The creep behavior can be described by a power law,

$$\dot{\epsilon} = \frac{A}{T} \cdot \exp\left(-\frac{Q}{R \cdot T}\right) \cdot \left(\frac{\sigma}{E}\right)^n \quad [2]$$

where R is the gas constant, Q is the activation energy, E is the Young's modulus, and A is a constant. This constant is obtained by fitting Eq. [2] to the experimental data using literature values^[18] for $Q_\alpha = 190 \text{ kJ} \cdot \text{mole}^{-1}$ and the shear modulus (converted to Young's modulus using a Poisson's ratio of 0.35^[19]), giving $A_{810^\circ\text{C}} = 4.9 \cdot 10^{16} \text{ K} \cdot \text{s}^{-1}$ and $n_{810^\circ\text{C}} = 2.4$. At 910 °C, the creep curve shows a gradually increasing stress exponent, so that the data for stresses below 0.6 MPa are best described by a stress exponent $n_{910^\circ\text{C}} = 2.9$, whereas the data for stresses above 0.8 MPa show $n_{910^\circ\text{C}} = 5.0$; the pre-exponential factors are $A_{910^\circ\text{C}} = 4.6 \cdot 10^{19} \text{ K} \cdot \text{s}^{-1}$ and $A_{910^\circ\text{C}} = 1.1 \cdot 10^{30} \text{ K} \cdot \text{s}^{-1}$, respectively using $Q_\beta = 184 \text{ kJ} \cdot \text{mole}^{-1}$.^[18]

Figure 3(a) and (b) show the temperature and strain history upon thermal cycling between $T_l = 810 \text{ }^\circ\text{C}$ and $T_u = 910 \text{ }^\circ\text{C}$, with a thermal cycling frequency of $\nu = 6 \text{ h}^{-1}$ at a stress of $\sigma = 0.34 \text{ MPa}$, followed by the isothermal strain history of β -Zr crept immediately after cycling, with the same stress at the upper cycling temperature, $T_u = 910 \text{ }^\circ\text{C}$. Despite the lower average temperature of the cycling experiments, the average strain rate upon thermal cycling ($\dot{\epsilon}_{\text{cyc}} = 3.9 \cdot 10^{-6} \text{ s}^{-1}$) is 10 times higher than the isothermal creep rate of β -Zr ($\dot{\epsilon}_{910^\circ\text{C}} = 4.0 \cdot 10^{-7} \text{ s}^{-1}$).

The strain increment per cycle, $\Delta\epsilon_{\text{tot}} = \Delta D/L$ (where $\Delta D = \Delta L$ is the deformation increment of the sample gage for a full cycle and L is the gage length at the beginning of the cycle) is shown in Figure 4 as a function of the applied stress for cycles with $T_l = 810 \text{ }^\circ\text{C}$, $T_u = 910$ to $940 \text{ }^\circ\text{C}$, and $\nu = 6$ to 30 h^{-1} . Cycling data measured when the sample strain was under 56 pct are not given in Figure 4

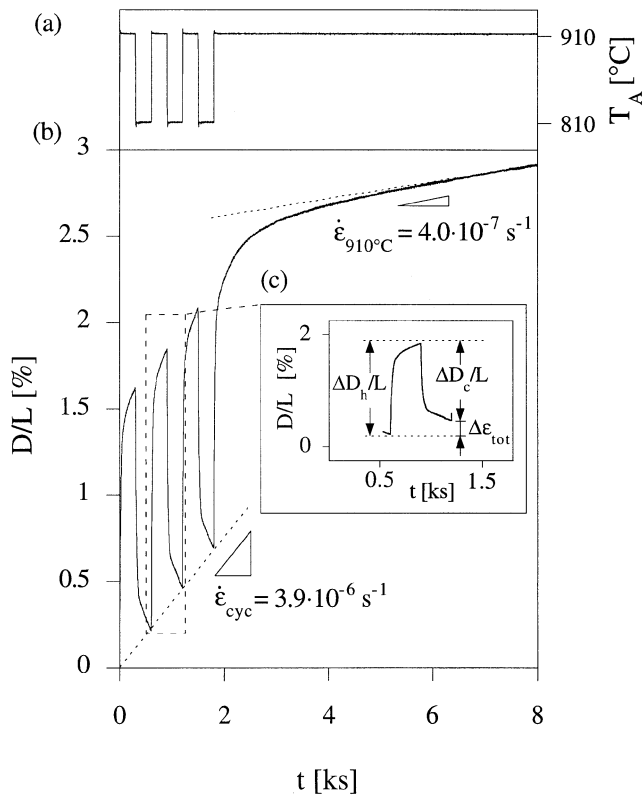


Fig. 3—(a) Temperature and (b) strain as a function of time for cycling between $T_l = 810^\circ\text{C}$ and $T_u = 910^\circ\text{C}$ with $\nu = 6\text{ h}^{-1}$ under constant stress $\sigma = 0.34\text{ MPa}$. Isothermal creep at $T_u = 910^\circ\text{C}$ followed the cycling segment. (c) Single thermal cycle.

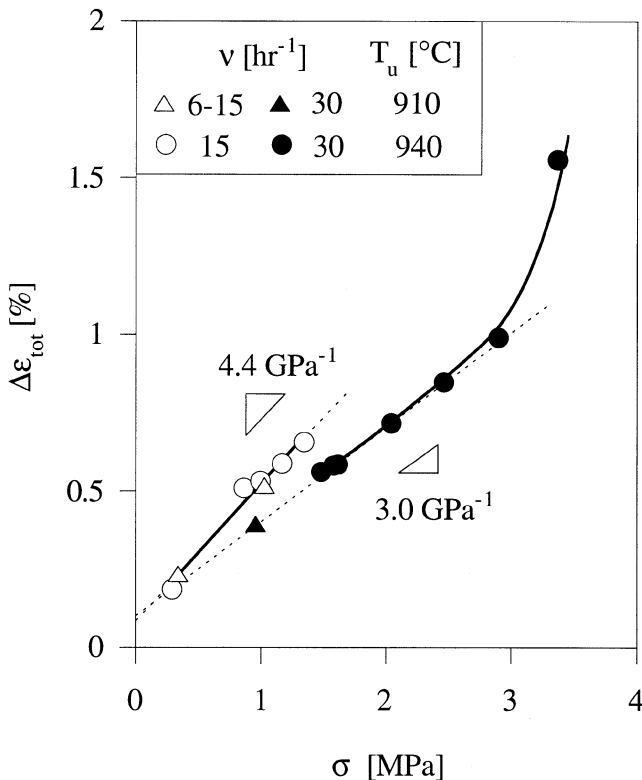


Fig. 4—Total strain increment per cycle as a function of the applied stress for cycles with $T_l = 810^\circ\text{C}$, $T_u = 910$ to 940°C , and $\nu = 6$ to 30 h^{-1} .

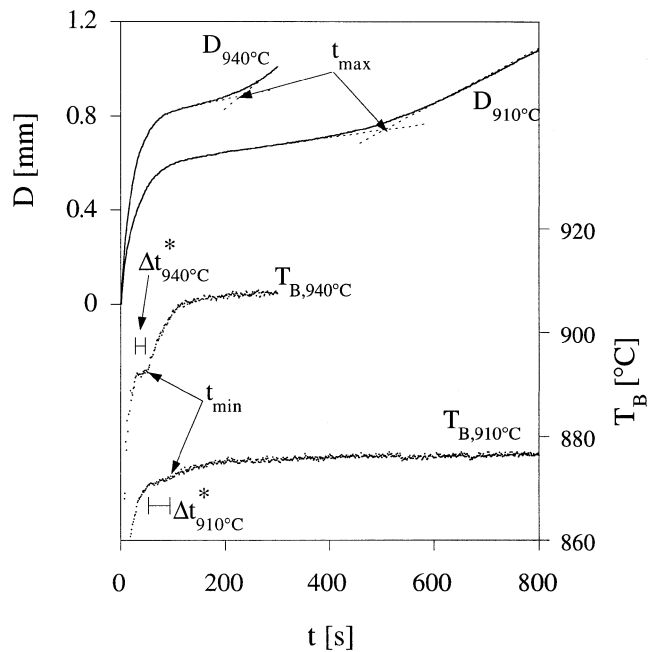


Fig. 5—Deformation D and temperature T_B as a function of time for heating from $T_l = 810^\circ\text{C}$ to $T_u = 910^\circ\text{C}$ or $T_u = 940^\circ\text{C}$ at a stress $\sigma = 1.1\text{ MPa}$. The temperature used in index is T_A , the upper cycling temperature applied at the sample gage section.

because, before that point, the stress-normalized cyclic strain increments were slowly but systematically decreasing, most probably as a result of grain growth in the sample. Figure 4 shows that, at frequencies below $\nu = 30\text{ h}^{-1}$, the strain increment increases linearly with the applied stress up to $\sigma = 1.4\text{ MPa}$, with a slope of $d(\Delta\epsilon_{\text{tot}})/d\sigma = 4.4\text{ GPa}^{-1}$. A linear fit of the data gives an extrapolated strain value of $\Delta\epsilon_0 = 0.08\text{ pct}$ when no stress is applied. At $\sigma = 1\text{ MPa}$, several points measured at frequencies of $\nu = 6$ to 15 h^{-1} overlap. Upon cycling with a high frequency of $\nu = 30\text{ h}^{-1}$, smaller strain increments are observed, leading to a slope of $d(\Delta\epsilon_{\text{tot}})/d\sigma = 3.0\text{ GPa}^{-1}$ up to $\sigma = 2.9\text{ MPa}$, after which a significantly higher strain increment, $\Delta\epsilon_{\text{tot}} = 1.6\text{ pct}$, is obtained for the maximum stress of 3.4 MPa .

The points shown in Figure 4 are averages of four to six total cycle strain increments. Over multiple cycles, the deformation increment showed only a very small standard deviation (the reproducibility of the deformation upon thermal cycling is illustrated in Figure 3(b)). However, the length of the sample was calculated assuming conservation of the volume of the gage section without sample head deformation or necking. The systematic error due to these simplifying assumptions increases with the extent of plastic deformation and was estimated by comparing the gage length, calculated as the sum of the deformation increments (including the deformation of the sample heads), with the measured gage length of the deformed sample at the end of the experiment. Accordingly, the uncertainties are $\pm 5\text{ pct}$ for the strain and $\pm 8\text{ pct}$ for the stress.

Figure 5 depicts the deformation history ($D(t)$), for an applied stress of $\sigma = 1.1\text{ MPa}$, for two heating segments, as measured with the linear voltage displacement transducer, and the corresponding temperature ($T_B(t)$), as measured at the shoulder of the sample head. (Figures 1(b) and (c)), for upper cycling temperature $T_u = T_A = 910^\circ\text{C}$ and

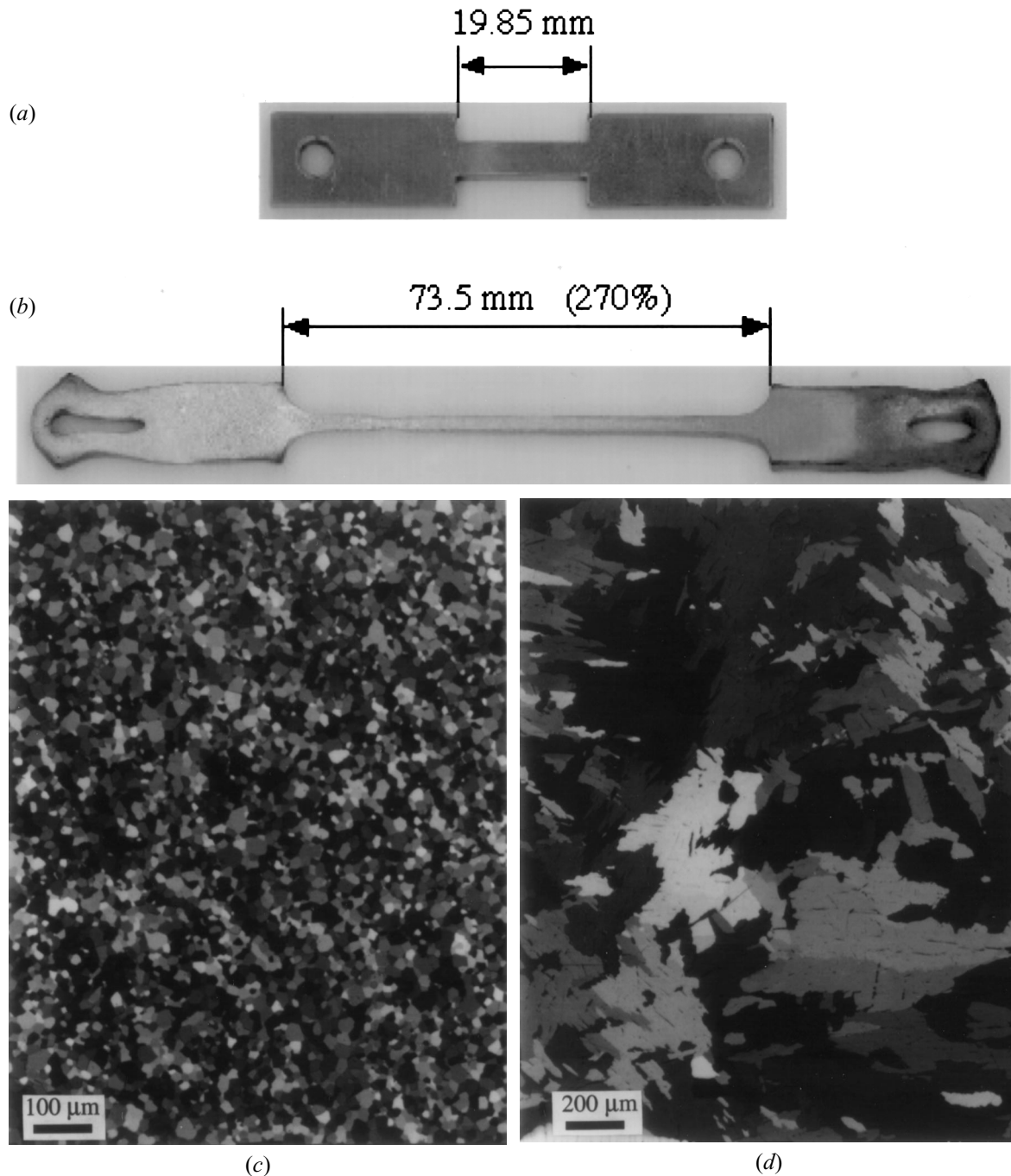


Fig. 6—Zirconium sample (a) in the undeformed state and (b) at the end of the experiment, after deformation by both transformation superplasticity and isothermal creep at various stresses. (c) and (d) Corresponding micrographs of the gage section in the direction of the applied stress.

940 °C. The surface gage section temperature (controlling thermocouple A) reaches its final value very rapidly ($dT/dt = 10$ to $15 \text{ K} \cdot \text{s}^{-1}$), as shown in Figure 3(a).

Figure 6 shows the sample before the experiment (Figure 6(a)) and after a total engineering of strain $e = 270$ pct (Figure 6(b)) had been accumulated without fracture at the end of the experiment. The strain accumulated during all isothermal creep segments was 40 pct (16 pct for the first part of the experiment and 24 pct for the creep segments in the other parts), while the strain accumulated during the cycling superplastic segments was 230 pct. Metallography of the undeformed sample (Figure 6(c)) revealed equiaxed grains typical of a cold-worked, recrystallized structure

with a grain size of $d = 19 \pm 2 \mu\text{m}$. The deformed sample (Figure 6(d)) showed large, coarsened grains ($d = 0.2$ to 2 mm), typical of a transformed β structure. Except for hydrogen, the concentrations of interstitial elements increased only a little during the 25-hour experiment (Table I). Hydrogen probably originated from traces of water in the argon gas, decomposing over the titanium bed where oxygen was preferentially gettered, thus increasing the hydrogen concentration in the cover gas, which was then absorbed by the zirconium sample. This slight contamination did not, however, affect the transformation superplastic behavior over the course of the experiment; furthermore, hydrogen can easily be removed from zirconium by a vacuum anneal.

IV. DISCUSSION

A. Isothermal Creep

Figure 2 shows that the isothermal creep of bcc β -Zr is significantly faster at 910 °C than for hcp α -Zr at 810 °C, as is expected from the higher temperature and the more open bcc structure of β -Zr and in agreement with the deformation mechanism map of zirconium by Sargent and Ashby.^[18] However, the stress exponent $n_{910^\circ\text{C}} = 5.0$, measured at high stresses for β -Zr, is somewhat higher than the reported value of $n = 4.3$ for power-law creep. This discrepancy may be due to the fact that the latter stress exponent was not experimentally measured, but assumed by Sargent and Ashby^[18] to be equal to that for isomechanical β -Ti. The calculated transition between diffusional creep and power-law creep (expected to occur for β -Zr at $\sigma = 1.0$ MPa for a grain size of $d = 0.2$ mm and at $\sigma = 0.25$ MPa for a grain size of $d = 2$ mm^[18]) is in agreement with the observed gradual decrease of the stress exponent below about $\sigma = 0.8$ MPa.

The stress exponent $n_{810^\circ\text{C}} = 2.4$ for α -Zr (measured over the narrow stress range of interest for the present cycling experiments) is much lower than the experimental literature value for power-law creep of cold-rolled and annealed α -Zr ($n = 6.6$ ^[18]). As for β -Zr, this intermediate value for the stress exponent of α -Zr is attributed to a change of the deformation mechanism from power law to diffusional creep. For the as-received grain size of 19 μm , the two mechanisms contribute equally to the overall strain rate at a stress of 8.1 MPa.^[18] Grain growth is, however, expected to occur rapidly, as the sample is a pure metal at a homologous temperature of 0.51, so that grain sizes in the range of $d = 0.2$ to 2 mm can be expected, for which a stress range for the mechanism transition is $\sigma = 1.4$ to 3.2 MPa,^[18] close to the stress range investigated in Figure 2.

B. Thermal Cycling

1. Experiment design

The experimental setup (Figure 1) was designed to minimize deformation of zirconium in the β range, where creep is rapid (Figure 2). While the large sample heads were mostly shielded by the pull heads from the radiative heat flux (Figures 1(b) and (c)), the gauge section was fully exposed to the radiation, so that heat flow to the sample occurred predominantly through the surface of the gauge section. Conversely, on cooling, little heat was lost by conduction through the alumina pins and spacers and the low-conductivity superalloy load train (Figure 1(c)), so that heat transfer occurred mostly by radiation from the gauge surface.

During the allotropic phase change, the heat flux must provide the transformation enthalpy. The time for the complete transformation of the sample is, thus, proportional to the ratio of the volume to be transformed (full sample volume, including gauge section and sample heads) and the area of the heat-flux surface (gauge section surface area only). Since heat flows predominantly through the gauge section, the transformation of the sample heads occurs by conduction of heat from and to the sample gauge section. Given that the initial volume-to-surface area ratio for the gauge section ($V_g/S_0 = 1.2$ mm) is small compared to the ratio of the head volume to the gauge area ($V_h/S_0 = 8.8$ mm), the gauge section transforms much more rapidly than the large

sample heads. However, since conduction is not limiting, the temperature in the bulk of the gauge section remains constant at the phase transformation temperature until the sample heads are fully transformed, except for the surface, where the surface temperature (T_s) is given by the boundary condition $T_s = T_A$. The slowly transforming heads, thus, act as heat sinks on heating and heat reservoirs on cooling after the gauge section has fully transformed. By using cycle periods longer than the time interval necessary to complete the phase transformation in the gauge section but shorter than the time interval necessary to transform the whole sample, the sample temperature can be maintained at the allotropic temperature $T_{\alpha/\beta}$, thus minimizing excessive creep in the β range. This heat-buffer technique is also potentially interesting for commercial superplastic forming, as it allows a passive control of the temperature and minimizes creep in the weak allotropic phase.

2. Transformation times

The heat-transport analysis is based on the assumption that (1) heat transfer is by radiation only, (2) the absorptivity and emissivity of the sample are $\alpha' = \epsilon' = 0.5$, and (3) thermal gradients are negligible within the material. The latter assumption is validated by calculating the dimensionless number M ,^[20] which is equivalent to the Biot number for conductive heat transport and is defined as

$$M = \frac{\sigma_B \cdot \alpha' \cdot T^3 \cdot x}{k} \quad [3]$$

where σ_B is the Stefan-Boltzmann constant, α' is the absorptivity on heating (to be replaced by the emissivity ϵ' on cooling), k is the thermal conductivity and x is the characteristic distance, which is half the sample gauge section width for the transformation of the gauge section or the full head length for the transformation of the heads. With k (860 °C) = 25 W · m⁻¹ · K⁻¹,^[19] $\alpha' = 0.5$, $T = 940$ °C, $x = 2.55$ mm for the gauge section and $x = 28.1$ mm for the sample head, Eq. [3] gives values for M smaller than 0.1 ($M = 0.005$ and 0.06, respectively), so that thermal gradients within the material are negligible and conduction does not control the heat transport (Newtonian conditions). The absence of macroscopic thermal gradients within the material also excludes the deformation by ratchetting observed during allotropic cycling of, *e.g.*, uranium^[21], with a sharply defined phase front.

In Figure 5, the temperature T_B , as measured at the sample head surface, increases until the onset of the phase transformation, where the rate of heating is reduced to near zero due to the absorption of heat supporting the transformation enthalpy. After the gauge section has transformed (marked as t_{\min} in Figure 5), the heating rate measured at point B increases again until the temperature levels off at about 30 °C below the upper cycling temperature specified by T_A . The preceding interpretation (*i.e.*, that the temperature T_B is largely constant during the transformation of the sample gauge section, but increases during the transformation of the sample heads) can be justified as follows.

Over the short time period corresponding to the gauge transformation, the temperature at the thermocouple tip B is controlled by the sample temperature, which is constant due to the phase transformation; however, over the long time period where the sample heads transform, the heating contribution from the heat flux to the thermocouple mantle

Table II. Transformation Times as Obtained Experimentally (Illustrated in Figure 5) and as Predicted (Equation [4]).

	$\Delta t_{910^\circ\text{C}}^*$ (s)		$\Delta t_{940^\circ\text{C}}^*$ (s)	
	Figure 5	Eq. [4]	Figure 5	Eq. [4]
Heating ($T_s = T_u$)	32.8 ± 3.9	31.3	24.3 ± 3.2	19.5
Cooling ($T_s = T_l$)	34.0 ± 1.2	33.6	34.3 ± 2.6	31.7

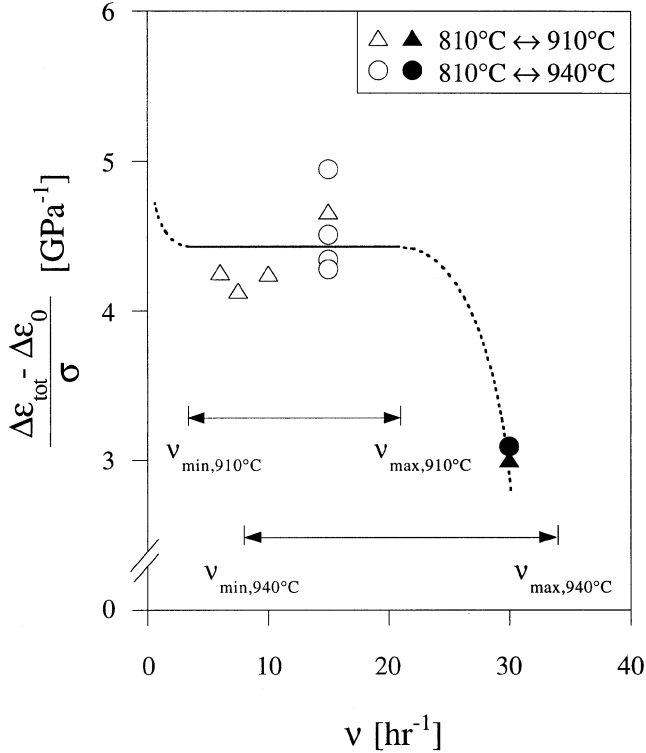


Fig. 7—Adjusted total strain increment per cycle normalized by the applied stress as a function of the cycling frequency for cycles with $T_l = 810^\circ\text{C}$, $T_u = 910$ to 940°C and stresses $\sigma = 0.9$ to 1.6 MPa. The symbols are the same as in fig. 4.

and tip becomes dominant and the thermocouple tip temperature T_B rises again, despite the constant sample temperature. As expected, the value of T_B at the transformation plateau increases with increasing flux, which is proportional to $T_u^4 - T_{\alpha/\beta}^4$ (Figure 5). Also, T_B is lower than T_A , because thermocouple B is further from the focus line of the heaters than thermocouple A, which is located at the gage section surface. Thus, the thermocouple temperature measured at position B (Figures 1(b) and (c)) is affected both by the heat flux due to transformation and the impinging radiation.

Under Newtonian conditions where thermal gradients are not sustainable within the material, the time (Δt^*) to transform a volume (V) by a radiative heat-transfer mechanism through a surface (S) is

$$\Delta t^* = \frac{\Delta H \cdot \rho}{\sigma_B \cdot \alpha' \cdot (T_s^4 - T_{\alpha/\beta}^4)} \cdot \frac{V}{S} \quad [4]$$

where $\Delta H = \pm 38.8 \text{ J} \cdot \text{g}^{-1}$ [22] is the enthalpy of transformation (positive on heating and negative on cooling), $\rho = 6.49 \text{ g} \cdot \text{cm}^{-3}$ [23] is the density of zirconium, and T_s is the surface temperature ($T_s = T_u$ on heating and $T_s = T_l$ on

Table III. Minimum Time t_{\min} as Obtained from $T_B(t)$ and Maximum Time t_{\max} as Obtained from $D(t)$ as Illustrated in Figure 5

	t_{\min} (s)		t_{\max} (s)	
	$T_A = 910^\circ\text{C}$	$T_A = 940^\circ\text{C}$	$T_A = 910^\circ\text{C}$	$T_A = 940^\circ\text{C}$
Heating	85.3 ± 5.1	51.5 ± 2.1	510	225 ± 5
Cooling	44.4 ± 0.9	52.7 ± 0.3	*	*

*Not detectable.

cooling). Although the tungsten filaments of the radiant heaters operate at a very high temperature, the heat flux to the sample surface is closed-loop-controlled by thermocouple T_A maintained at temperature T_s , and is, thus, equivalent to the flux from a furnace surrounding the sample and radiating at a temperature of $T_s = T_A$. The volume-to-surface area ratio in Eq. [4] can be found as a function of the engineering strain e by conservation of volume,

$$\frac{V}{S} = \frac{1}{\sqrt{1+e}} \cdot \frac{V_0}{S_0} \quad [5]$$

where $V_0/S_0 = 1.19 \text{ mm}$ is the initial ratio of the gage section. The transformation times predicted by using Eqs. [4] and [5] are in good agreement with experimentally determined transformation times, as seen from Table II, where averages are taken from four measurements. Although the predicted time for transformation (Eq. [4]) depends on several assumptions (e.g., $\alpha' = \epsilon' = 0.5$), the values for Δt^* are reasonable, so that the time t_{\min} in Figure 5 can indeed be taken as the minimum time needed to heat the sample from T_l to $T_{\alpha/\beta}$ and to transform its gage section.

This time, t_{\min} depends on the cycle characteristics (T_l , T_u , and ν) and is given in Table III for $T_u = T_A = 910^\circ\text{C}$ and $T_u = T_A = 940^\circ\text{C}$. The minimum cycling period for a complete transformation of the gage length is estimated to be $2 \cdot t_{\min}$ (taking the larger t_{\min} value of heating and cooling from Table III), so that the maximum cycling frequency is $\nu_{\max} = (2 \cdot t_{\min})^{-1} = 21 \text{ h}^{-1}$ for cycles with $T_u = 910^\circ\text{C}$. At cycle frequencies above this limit, the superplastic strain is expected to decrease, as the gage does not undergo a complete transformation. The cycle frequency varied between $\nu = 6$ and 30 hr^{-1} at $T_u = 910^\circ\text{C}$, for a constant stress of $\sigma = 1.0$ MPa (Figure 7). By subtracting the extrapolated strain per cycle when no external stress is applied ($\Delta\epsilon_0$) from the total strain per cycle and normalizing by the applied stress, i.e., $(\Delta\epsilon_{\text{tot}} - \Delta\epsilon_0)/\sigma$, the single-stress results can be directly compared to the slope $d(\Delta\epsilon_{\text{tot}})/d\sigma$, obtained by varying the stress (Figure 4).

At $T_u = 910^\circ\text{C}$, the strain increment per cycle normalized by the stress $d(\Delta\epsilon_{\text{tot}})/d\sigma = 4.4 \pm 0.3 \text{ GPa}^{-1}$ is constant between $\nu = 6$ and 15 h^{-1} , but decreases to $3.0 \pm 0.1 \text{ GPa}^{-1}$ at $\nu = 30 \text{ h}^{-1}$. This is because, at frequencies above $\nu_{\max} = 21 \text{ h}^{-1}$, only partial transformation occurs in the gage section, so that the internal mismatch and, thus, the superplastic strain increments, are reduced. When the upper cycle temperature is increased to $T_u = 940^\circ\text{C}$, the critical frequency is increased to $\nu_{\max} = (2 \cdot t_{\min})^{-1} = 34 \text{ h}^{-1}$. In contrast, the experimental data show a reduction of $d(\Delta\epsilon_{\text{tot}})/d\sigma$ already occurring at about $\nu = 30 \text{ h}^{-1}$. This value is lower than predicted, probably because of the effect

of high cycle frequencies on the actual cycle temperatures: the sample is not given enough time to cool to the lower temperature or to heat to the upper temperature, thus decreasing the effective temperature amplitude, as discussed in more detail later.

The deformation histories in Figure 5 show first the thermal expansion of the load train, followed by a decreasing expansion rate as the sample temperature is stabilized by the phase transformation of the large sample heads. During that time interval, the gage section, which is fully transformed at t_{\min} , is slowly creeping near the phase transformation temperature $T_{\alpha/\beta}$, as internal thermal gradients are not sustainable. The onset of accelerated expansion (marked as t_{\max} in Figure 5) is interpreted as the end of the phase transformation of the sample heads, where both thermal expansion and sample creep occur.

At low cycling frequencies, significant strain will be accumulated due to creep outside the phase transformation range, causing an increase of the total strain increment ($\Delta\varepsilon_{\text{tot}}$). According to Figure 7, this occurs at $\nu_{\min} = (2 \cdot t_{\max})^{-1} = 8.0 \text{ h}^{-1}$ for cycles with $T_u = T_A = 940 \text{ }^\circ\text{C}$ and $\nu_{\min} = (2 \cdot t_{\max})^{-1} = 3.5 \text{ h}^{-1}$ for $T_u = T_A = 910 \text{ }^\circ\text{C}$ (dotted lines in Figure 7). The results for t_{\max} are given in Table III, where the single data point $t_{\max}(T_A = 910 \text{ }^\circ\text{C})$ was obtained during isothermal creep at the end of thermal cycling and $t_{\max}(T_A = 940 \text{ }^\circ\text{C})$ is the average of four cycles with a cycle frequency of $\nu = 6 \text{ h}^{-1}$. Since the measurements with a slope of $d(\Delta\varepsilon_{\text{tot}})/d\sigma = 4.4 \text{ GPa}^{-1}$ in Figure 4 were performed at rates falling within the window given by ν_{\min} and ν_{\max} , the measured superplastic strain increments correspond to complete transformation of a gage length, with an insignificant creep contribution after transformation plasticity.

A final check is performed by calculating the ratio of the time to transform the whole sample ($t_{\max} - t_{\min} + \Delta t^*$) to the time for gage transformation. With experimental data from Table II, this ratio is 14 at $910 \text{ }^\circ\text{C}$ and 8 at $940 \text{ }^\circ\text{C}$, reasonably close to the ratio of 8.3 for the total sample volume to the gage section volume.

3. Cycle strains

To the best of our knowledge, only two other studies exist on the transformation superplasticity of zirconium. An early investigation was carried out by Lozinsky^[13] under nonuniform temperature conditions, giving only a qualitative description of the effect. Greenwood and Johnson^[18] performed a systematic study for zirconium cycled between $810 \text{ }^\circ\text{C}$ and $910 \text{ }^\circ\text{C}$ and reported a linear strain increment–stress behavior up to $\sigma = 1 \text{ MPa}$ (with a slope of $d(\Delta\varepsilon_{\text{tot}})/d\sigma = 9.0 \text{ GPa}^{-1}$, significantly higher than that in Figure 4), becoming progressively nonlinear up to a maximum strain increment of $\Delta\varepsilon_{\text{tot}} = 1.9 \text{ pct}$ at $\sigma = 1.4 \text{ MPa}$. Although these results are qualitatively consistent with the present data (linear stress-strain correlation at small stresses followed by a nonlinear increase), direct comparison is impossible since Greenwood and Johnson stated neither cycle frequency nor grain size, so that the creep contribution outside the phase transformation range at higher stresses is unknown. Additional possible causes for their higher strain increments in the linear range are the presence of primary creep (if no creep deformation was performed prior to cycling) and the contribution of diffusional creep (if the grain size was not stabilized). The latter effect may also explain

the decreasing strain increment (from $\Delta\varepsilon_{\text{tot}}/\sigma = 8.5 \text{ GPa}^{-1}$ to $\Delta\varepsilon_{\text{tot}}/\sigma = 5.0 \text{ GPa}^{-1}$, not shown in Figure 4) observed during the second part of our experiment.

The theoretical models relate the physical properties of the transforming material ($\Delta V/V$, σ_0 , A , Q , and n) to the plastic strain induced by a single phase transformation during a half cycle. However, the plastic strain increments measured over a whole cycle (Figure 3) include plastic strains caused by both phase transformations on heating and cooling, which are not necessarily equal. We examine this issue in the following text.

The load-train displacement measured at the end of each half cycle on heating (ΔD_h) and on cooling (ΔD_c) (Figure 3(b)) consists of the following three contributions:

$$\Delta D_{h,c} = \pm \Delta D_{\text{cte}} + \Delta D_{\text{creep}} + \Delta D_{\text{tp}} \quad [6]$$

where ΔD_{cte} is the magnitude of the displacement of the load train due to the thermal expansion on heating or contraction on cooling, ΔD_{creep} is the displacement due to sample creep outside the phase transformation range, and ΔD_{tp} is the displacement caused by transformation plasticity. While ΔD_{cte} is fully reversible over a whole thermal cycle, ΔD_{creep} and ΔD_{tp} give irreversible plastic strains at the end of each half cycle. At low stresses where ΔD_{creep} is small compared to ΔD_{tp} (Figure 3(a)) and ΔD_{tp} is linearly dependent on the applied stress, Eq. [6] can be approximated by

$$\Delta D_{h,c} \approx \pm \Delta D_{\text{cte}} + \frac{d(\Delta\varepsilon_{h,c})}{d\sigma} \cdot L \cdot \sigma \quad [7]$$

where $\Delta\varepsilon_{h,c}$ is the strain increment per transformation (h representing heating and c representing cooling) and L is the gage length of the sample. Thus, the slope of ΔD_h or ΔD_c as a function of $L \cdot \sigma$ gives the stress-normalized strain increment $d(\Delta\varepsilon_{h,c})/d\sigma$ for transformation on heating and cooling, respectively, as shown in Figure 8, where $d(\Delta\varepsilon_h)/d\sigma = 2.4 \text{ GPa}^{-1}$ and $d(\Delta\varepsilon_c)/d\sigma = 2.0 \text{ GPa}^{-1}$. Although the slightly higher value on heating may be due to creep outside the transformation range, the difference in the slope and in the intercepts at zero stress are within experimental error (5 pct on strain and 8 pct on stress). Thus, the strain increment per transformation on heating (α/β) and cooling (β/α) are equal for a given stress ($\Delta\varepsilon_h = \Delta\varepsilon_c = \Delta\varepsilon$) with $d(\Delta\varepsilon)/d\sigma = 2.2 \pm 0.2 \text{ GPa}^{-1}$, as predicted by the linear theory (Eq.[1]). It is assumed that this also holds for the nonlinear stress region described in References 14 through 16.

Because of its hcp structure, α -Zr exhibits different coefficients of thermal expansion for the basal plane and for its normal direction, so that the corresponding thermal strains are also a source of internal mismatch. The models developed for transformation plasticity can be used for anisotropic thermal expansion mismatch by introducing an equivalent volumetric mismatch $(\Delta V/V)_{\text{eq}}$, as follows:^[15]

$$\left(\frac{\Delta V}{V}\right)_{\text{eq}} = K_1 \cdot \overline{\Delta\alpha_m} \cdot \overline{\Delta T_{pl}} \quad [8]$$

where $\overline{\Delta\alpha_m}$ is the temperature-averaged difference between the coefficients of thermal expansion in the two directions, $\overline{\Delta T_{pl}}$ is the effective temperature amplitude causing plasticity, and K_1 is a correction factor incorporating the nonideality of the simple form of Eq. [8]. For α -uranium and

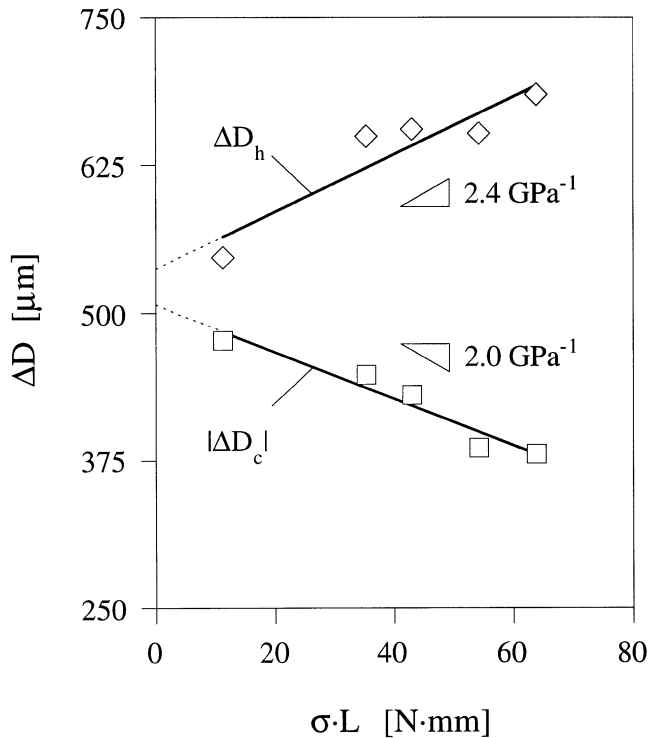


Fig. 8—Deformation difference of the heating and cooling part of the temperature cycle (Fig. 3(c)) as a function of the product of the applied stress with the instantaneous sample length for cycles with $T_1 = 810$ °C, $T_u = 940$ °C, $\nu = 15$ h⁻¹, and $\sigma = 0.3$ to 1.3 MPa.

zinc, K_1 takes a value of 0.2¹⁵. The thermal mismatch strain $\overline{\Delta\alpha_m} \cdot \overline{\Delta T_{pl}}$ can be estimated directly from the thermal dilatation curve.^[24] Neglecting any elastic accommodation, the difference between the thermal strains ($\Delta L/L_{20^\circ\text{C}}$) parallel to the c -axis and parallel to the a -axis is $\epsilon_{c,863^\circ\text{C}} - \epsilon_{a,863^\circ\text{C}} = 0.49$ pct at $T_{\alpha\beta} = 863$ °C and $\epsilon_{c,810^\circ\text{C}} - \epsilon_{a,810^\circ\text{C}} = 0.43$ pct at $T_1 = 810$ °C, giving $\overline{\Delta\alpha_m} \cdot \overline{\Delta T_{pl}} = 0.06$ pct. Thus, the equivalent thermal expansion mismatch is $(\Delta V/V)_{eq} = 0.012$ pct, which is negligible compared to the phase transformation mismatch $\Delta V/V = 0.41$ pct,^[24] so that thermal expansion mismatch superplasticity can be ruled out in the present case.

C. Internal Stress

1. Complete transformation

Greenwood and Johnson^[8] developed a model for transformation superplasticity where internal strain accommodation is by creep. In their derivation, they expressed the von Mises criterion in terms of strain rates, which they integrated over the time of transformation to relate the internal strains with the average internal stress. By requiring compatibility of strains in the z direction, where the external stress is applied, and by using invariant properties of the $\Delta V/V$ tensor, they obtained

$$\sigma'_{zz} = \frac{\sigma_0 \cdot [\Delta\epsilon - (\Delta V/V)_{zz}]}{(\Delta V/V) \cdot \left[1 + \frac{9 \cdot (\Delta\epsilon)^2}{4 \cdot (\Delta V/V)^2} - \frac{9 \cdot \Delta\epsilon \cdot (\Delta V/V)_{zz}}{2 \cdot (\Delta V/V)^2} \right]^{\frac{(n-1)}{2n}}} \quad [9]$$

where $(\Delta V/V)_{zz}$ and σ'_{zz} are the zz components of the mismatch tensor and deviatoric stress tensor respectively, and the average internal stress is given by

$$\sigma_0 = E \cdot \left[\frac{2}{3} \cdot \frac{\Delta V/V}{\Delta t^* \cdot \frac{A}{T_{\alpha\beta}} \cdot \exp\left(-\frac{Q}{R \cdot T_{\alpha\beta}}\right)} \right]^{1/n} \quad [10]$$

Defining the average of a function g over a spherical volume element within $\vartheta = \varphi = [0; \pi/2]$ as

$$\bar{g} = \frac{\int_{\Omega} g \, d\Omega}{\int_{\Omega} d\Omega} \quad [11]$$

both sides of Eq. [9] can be averaged:

$$\overline{\Psi} = (\eta - \gamma) \cdot \left(1 + \frac{9}{4} \cdot \eta^2 - \frac{9}{2} \cdot \eta \cdot \gamma \right)^{\frac{(1-n)}{2n}} \quad [12]$$

where the dimensionless plastic strain is defined as $\eta = \Delta\epsilon/(\Delta V/V)$, the dimensionless deviatoric stress as $\Psi = \sigma'_{zz}/\sigma_0$, and the dimensionless mismatch strain as $\gamma = (\Delta V/V)_{zz}/(\Delta V/V)$, with $\gamma = (1/3) \cdot \cos(\varphi)^2 \cdot \sin(\vartheta)^2 + (1/3) \cdot \sin(\varphi)^2 \cdot \sin(\vartheta)^2 - (2/3) \cdot \cos(\vartheta)^2$, obtained by relating the volumetric mismatch $\Delta V/V$ to $(\Delta V/V)_{zz}$ (Reference 8).

The left-hand side of Eq. [12] is given by $\overline{\Psi} = (2/3) \cdot (\sigma/\sigma_0)$, while integration of the nonlinear right-hand side of Eq. [12] is only possible by numerical methods (as done by Mitter^[16]), except for two special cases. First, for $n = 1$, Eq. [12] becomes

$$\delta = \frac{3}{2} \cdot \eta \quad [13]$$

where the dimensionless stress is defined as $\delta = \sigma/\sigma_0$. Second, for $n \rightarrow \infty$, (*i.e.*, the ideal plastic limit), Eq. [12] becomes^[14,15]

$$\delta = \frac{1}{4} + \frac{1}{6 \cdot \eta} + \frac{1}{2\sqrt{2} \cdot \eta} \cdot \left(\frac{3 \cdot \eta}{4} - \frac{1}{6} - \frac{1}{9 \cdot \eta} \right) \cdot \ln \left[\frac{(3 \cdot \eta + 3\sqrt{2} \cdot \eta + 2)^2}{9 \cdot \eta^2 - 6 \cdot \eta + 4} \right] \quad [14]$$

For the case of small strains where $\Delta\epsilon \ll \Delta V/V$ (*i.e.*, $\eta \ll 1$), Greenwood and Johnson^[8] expanded the argument of the right-hand-side integral of Eq. [12] to obtain Eq. [1], expressed in dimensionless manner as

$$\delta \approx \frac{3}{2} \cdot \frac{(4 \cdot n + 1)}{5 \cdot n} \cdot \eta \quad [15]$$

Thus, the internal stress σ_0 can be determined by fitting experimental strain increment data to

- (1) Eq. [12], by numerical integration;
- (2) Eq. [13], for diffusional accommodation with $n = 1$;
- (3) Eq. [14], for power-law accommodation with a very high stress exponent ($n > 10$) over the whole range of stresses; and
- (4) Eq. [15], for power-law accommodation at small stresses ($\sigma \ll \sigma_0$).

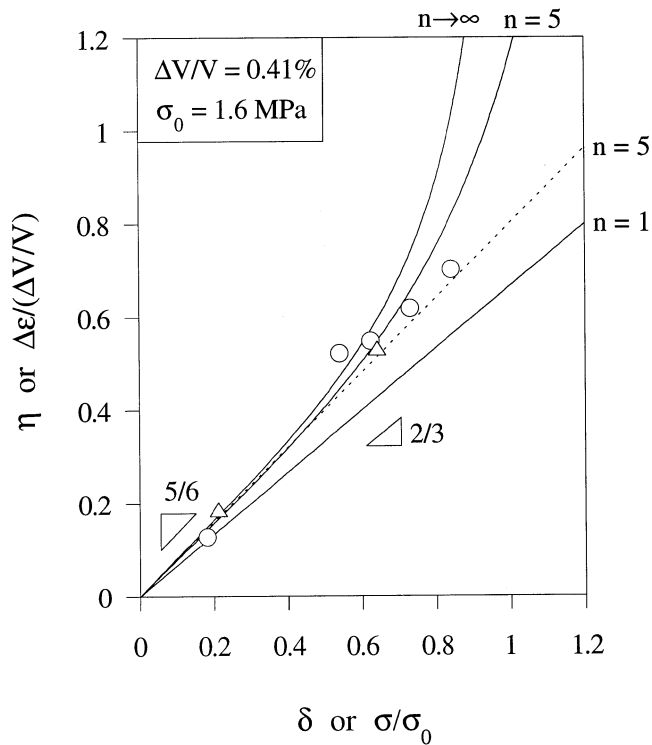


Fig. 9—Dimensionless strain increment per transformation as a function of the dimensionless stress. Experimental results for complete transformation (adjusted as described in the text and with the same symbols as in Fig. 4) are compared to model predictions for diffusional creep ($n = 1$, Eq. [13]), power-law creep ($n = 5$, Eq. [12] (full), and Eq. [15] (dotted)), and ideally plastic ($n \rightarrow \infty$, Eq. [14]).

Alternatively, the internal stress can be found from (5) Eq. [10], if the transformation time is known.

Because creep for zirconium in the stress range of interest occurs by a mixture of dislocation creep and diffusional creep with effective stress exponents between 2.9 and 5 (Figure 2), methods (2) and (3) cannot be used to calculate the internal stress. Furthermore, most of the measured strain increments are on the order of $\Delta V/V = 0.41$ pct (Figure 4), so that method (4) with Eq. [15] is strictly not possible. However, Eq. [15] has been used to model transformation superplasticity of creeping materials even at larger stresses and strains^{8,12} where Eq. [15] coincides with the numerical solutions (Eq. [12]). For cycles with complete transformation ($\nu < 30 \text{ h}^{-1}$ in Figure 4), we compare in Figure 9 the analytical and numerical solutions to the experimental data, for which the measured strain $\Delta \epsilon_{\text{tot}}$ was adjusted by subtracting the extrapolated zero-stress strain value $\Delta \epsilon_0$ and dividing by 2 to get the plastic strain increment per transformation (*i.e.*, $\Delta \epsilon = (\Delta \epsilon_{\text{tot}} - \Delta \epsilon_0)/2$), and the applied stress was normalized by the internal stress $\sigma_0 = 1.6$ MPa. The internal stress was determined from three of the previous methods, as described in the following text.

First, fitting the data to the numerical solution of Eq. [12] (method (1)) using a least-squares error technique gives an internal stress of $\sigma_0 = 1.6$ MPa for $\Delta V/V = 0.41$ pct for both $n = 2.9$ and $n = 5$, since the numerical solutions are not very sensitive to n at intermediate strain increments (*i.e.*, $0.5 < \eta < 0.7$), where most of the data were collected. Second, using method (4) with Eq. [15] beyond its nominal validity range, with $d(\Delta \epsilon)/d\sigma = 2.2 \pm 0.2 \text{ GPa}^{-1}$, gives σ_0

= 1.4 to 1.5 ± 0.1 MPa for stress exponents of $n = 2.9$ and $n = 5$, respectively. As expected, the latter values are close to that obtained from fitting to the numerical solution (method (1)), as both models coincide up to $\eta \approx 0.3$. However, the data with normalized strains between $\eta = 0.5$ to 0.7 (Figure 9) are consistently above the predictions by Eq. [15], which is due to the difference of $\Delta \sigma_0 = 0.15$ MPa found between the best fits for the linear model and the numerical integration. Although this difference is small (≈ 10 pct), it demonstrates the limitation of the linear model.

Finally, method (5) gives an internal stress of $\sigma_0 = 1.7$ to 1.5 MPa when Eq. [10] is used with the β -Zr activation energy ($Q_\beta = 184 \text{ kJ} \cdot \text{mole}^{-1}$ ^[18]), elastic modulus ($E_\beta = 51.7 \text{ GPa}$ at $863 \text{ }^\circ\text{C}$ ^[18]), creep exponent and constant ($n = 5.0$ and $A = 1.1 \cdot 10^{30} \text{ K} \cdot \text{s}^{-1}$), and the experimentally determined time periods for gauge transformation ($\Delta t^* = 24$ to 34 seconds) (Table II). When applying the lower stress exponent creep law at $910 \text{ }^\circ\text{C}$ (Eq. [2], with $A = 4.6 \cdot 10^{19} \text{ K} \cdot \text{s}^{-1}$ and $n = 2.9$ for $\sigma < 0.6$ MPa), internal stresses of $\sigma_0 = 3.5$ to 3.1 MPa are obtained. While these internal stress values are much higher than those obtained with methods (1) and (4) presented earlier, they are still reasonable given the approximations made in determining the time of transformation and the assumption that the plastic strain is accumulated only during that time period (*i.e.*, relaxation of the internal strains occurs quickly).

2. Partial transformation

Additional considerations must be taken into account to model the partial transformation data in Figure 4. High-frequency cycling causes a change of the internal stress because of the smaller effective temperature amplitude to which the sample is subjected, since heat transport to, and from, the sample surface is reduced. The resulting reduction in the thermal driving force for the phase transformation increases the time period Δt^* (Eq. [4], as shown for cycles with $T_u = 910 \text{ }^\circ\text{C}$ and $T_u = 940 \text{ }^\circ\text{C}$ in Table III), which would lead to a reduction of the internal stress, according to Eq. [10]. However, the volume mismatch which develops over the time Δt^* is also reduced. Without specific information about the relationship between the kinetics of the internal mismatch decay and the time of transformation at high cycle frequencies, a quantitative determination of the internal stress on the basis of Eq. [10] is not possible. In an attempt to quantify transformation superplasticity under rapid cycling conditions, a simple approach is to define, based on Eq. [1], an effective mismatch ($(\Delta V/V)_{\text{eff}}$) and an effective internal stress ($\sigma_{0,\text{eff}}$).

$$\left(\frac{\Delta V}{V}\right)_{\text{eff}} = \frac{1}{2} \cdot \left(\frac{\Delta V}{V} + z \cdot \frac{\Delta V}{V}\right) = \frac{1+z}{2} \cdot \frac{\Delta V}{V} \quad [16]$$

$$\sigma_{0,\text{eff}} = \frac{1}{2} \cdot \left(\sigma_0 + \frac{\sigma_0}{z}\right) = \frac{1+z}{2 \cdot z} \cdot \sigma_0 \quad [17]$$

where z is the ratio of $d(\Delta \epsilon_p)/d\sigma$ (the superplastic slope for partial transformation at a frequency ν) and $d(\Delta \epsilon)/d\sigma$ (the corresponding slope for complete transformation). Thus, Eqs. [16] and [17] are the averages of the extreme cases, where the reduction of $d(\Delta \epsilon)/d\sigma$ is due to either only a change in $\Delta V/V$ or only a change in σ_0 . From Figure 4, z

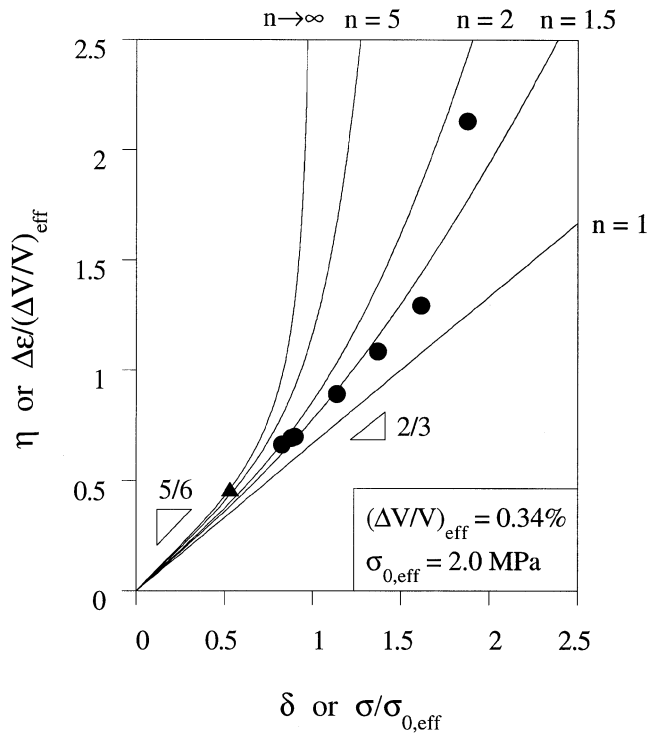


Fig. 10—Dimensionless strain increment per transformation as a function of the effective dimensionless stress. Experimental results for partial transformation are effective, adjusted values as described in the text and have the same symbols as in Fig. 4. Model predictions include diffusional creep ($n = 1$, Eq. [13]), power-law creep ($n = 1.5, 2, 5$, Eq. [12]), and ideally plastic ($n \rightarrow \infty$, Eq. [14]).

$= 3.0 \text{ GPa}^{-1}/4.4 \text{ GPa}^{-1} = 0.68$, so that $(\Delta V/V)_{\text{eff}} = 0.34$ pct (for $\Delta V/V = 0.41$ pct) and $\sigma_{0,\text{eff}} = 2.0$ MPa (for $\sigma_0 = 1.6$ MPa). Figure 10 shows the average effective dimensionless data for partial transformation together with analytical and numerical predictions. The data points are found to fit with the curves defined by $n = 1.5$ to 2. Although there is appreciable uncertainty regarding the exact value of the normalized data due to the somewhat arbitrary averaging procedure defined by Eqs. [16] and [17], the normalized results are significantly distinct from the curve defined by $n = 5$, even when extremes are considered, *i.e.*, either $(\Delta V/V)_{\text{eff}} = z \cdot (\Delta V/V)$ with σ_0 or $\sigma_{0,\text{eff}} = \sigma_0/z$ with $\Delta V/V$.

Since the phase transformation occurs over a stress range coinciding with the transition between diffusional creep ($n = 1$) and power-law creep ($n = 5.0$), the average transformation superplastic behavior might indeed be described by the intermediate stress exponent and pre-exponential factor, as suggested by the fit in Figure 10. Also, intermediate values for n and A conform with the results found for complete transformation (Figure 9), because the normalized transformation superplastic strain is largely insensitive to values of the stress exponent for $n = 1.5$ to 5 up to $\delta \approx 0.8$. This is in contrast to the case of a yielding material, where the strain increments, at an applied stress of 80 pct of the yield stress, are within the nonlinear region.^[10]

In summary, the partial transformation behavior observed at high cycle frequencies can be characterized only qualitatively with the existing data, although the main factors affecting transformation superplasticity have been identified. While the strain per cycle for a given stress is reduced

when transformation is incomplete, the average strain rate is increased because of the high cycling frequency. Also, higher applied stresses can be used before significant creep occurs, because the sample temperature is fixed at $T_{\alpha/\beta}$. Thus, high-frequency cycling can be used for rapid deformation by transformation superplasticity with large tensile strains, as confirmed by the total strain in excess of 100 pct accumulated during the parts of the experiment where rapid cycling was used.

V. CONCLUSIONS

1. Transformation superplasticity was demonstrated for polycrystalline zirconium with an engineering tensile strain of 270 pct without fracture. Strains per cycle as high as 1.6 pct and average strain rates of up to $1.3 \cdot 10^{-4} \text{ s}^{-1}$ were achieved with grain sizes as large as 2 mm.
2. Isothermal creep was measured for α -Zr at 810 °C and for β -Zr at 910 °C between 0.3 and 2 MPa, where deformation occurs by a mixture of diffusional and dislocation creep. A new technique was developed to minimize creep during thermal cycling outside the phase transformation range by using the transformation enthalpy of oversized sample heads as a heat buffer.
3. The transformation superplastic slope is $d(\Delta\epsilon)/d\sigma = 2.2 \text{ GPa}^{-1}$ for each α/β and β/α transformation, leading to a total value of $2 \cdot d(\Delta\epsilon)/d\sigma = 4.4 \text{ GPa}^{-1}$ for a full thermal cycle. Good agreement was found for the average internal allotropic stress as determined by two independent methods: first, by using the measured isothermal creep law and transformation times, and second, by using the experimentally determined transformation superplastic slope.
4. A window of cycle frequencies was found where the superplastic slope is independent of the cycling frequency, in agreement with predictions based on the transformation times and the temperature amplitudes.
5. High cycle frequencies reduced the superplasticity linear slope to $2 \cdot d(\Delta\epsilon)/d\sigma = 3.0 \text{ GPa}^{-1}$. This effect is explained by an incomplete gage transformation resulting in a decrease of the internal mismatch and an increase of the internal stress. The stress- and strain-normalized data can be fitted to β -Zr stress exponents between $n = 1.5$ and 2, corresponding to experimentally determined creep values.

ACKNOWLEDGMENTS

This study was supported by the United States Army Research Office under Grant No. DAAH004-95-1-0629 monitored by Dr. W.C. Simmons. The authors also acknowledge Dr. John Haygarth and Mr. Paul Danielson, Wah Chang (Albany, OR), for supplying and analyzing samples and for metallographic preparation, respectively.

REFERENCES

1. T.J. Nieh, J. Wadsworth, and O.D. Sherby: *Superplasticity in Metals and Ceramics*, Cambridge University Press, Cambridge, 1997.
2. D.C. Dunand and B. Derby: in *Fundamentals of Metal Matrix Composites*, S. Suresh, A. Mortensen, and A. Needleman, eds., Butterworth-Heinemann, Boston, MA, 1993, pp. 191-214.

3. R.C. Lobb, E.C. Sykes, and R.H. Johnson: *Met. Sci. J.*, 1972, vol. 6, pp. 33-39.
4. M.Y. Wu, J. Wadsworth, and O.D. Sherby: *Metall. Trans. A*, 1987, vol. 18A, pp. 451-62.
5. S.M. Pickard and B. Derby: *Scripta Metall.*, 1991, vol. 25, pp. 467-72.
6. A.G. Young, K.M. Gardiner, and W.B. Rotsey: *J. Nucl. Mater.*, 1960, vol. 2, pp. 234-46.
7. D.C. Dunand: *Int. Symp. on Superplasticity in Materials*, T. Chandra and T. Sakai, eds., TMS, Warrendale, PA, 1977, pp. 1821-30.
8. G.W. Greenwood and R.H. Johnson: *Proc. Roy. Soc. London*, 1965, vol. 283, pp. 403-22.
9. F.W. Clinard and O.D. Sherby: *Acta Metall.*, 1964, vol. 12, pp. 911-19.
10. P. Zwigl and D.C. Dunand: *Metall. Mater. Trans. A*, 1998, vol. 29A, pp. 565-75.
11. J.P. Poirier: *J. Geophys. Res.*, 1982, vol. 87, pp. 6791-97.
12. D.C. Dunand and C.M. Bedell: *Acta Metall. Mater.*, 1996, vol. 44, pp. 1063-76.
13. M.G. Lozinsky: *Acta Metall.*, 1961, vol. 9, pp. 689-94.
14. F.D. Fischer: *Acta Metall. Mater.*, 1990, vol. 38, pp. 1535-46.
15. P. Zwigl and D.C. Dunand: *Acta Mater.*, 1997, vol. 45, pp. 5285-94.
16. W. Mitter: *Umwandlungsplastizität und ihre Berücksichtigung bei der Berechnung von Eigenspannungen*, Gebr. Bornträger, Berlin, 1987, pp. 40-44.
17. H. Baker Ed.: *Alloy Phase Diagrams*, ASM, Materials Park, OH, 1992, vol. 3, pp. 4-8.
18. P.M. Sargent and M.F. Ashby: *Scripta Metall.*, 1982, vol. 16, pp. 1415-22.
19. *Metals Handbook: Properties and Selection: Nonferrous Alloys and Pure Metals*, ASM, Metals Park, OH, 1979, pp. 826-31.
20. D.R. Geiger and G.H. Poirier: *Transport Phenomena in Materials Processing*, TMS, Warrendale, PA, 1994, p. 407.
21. J.J. Stobo: *J. Nucl. Mater.*, 1960, vol. 2, pp. 97-109.
22. J. Shackelford and W. Alexander: *The CRC Materials Science and Engineering Handbook*, CRC Press, Boca Raton, FL, 1992, p. 268.
23. E.A. Brandes and G.B. Brook: *Smithells Metals Reference Book*, Butterworth-Heinemann, Oxford, United Kingdom, 1992, vol. 1, pp. 14-2.
24. *Thermophysical Properties of Matter*, Y.S. Touloukian, R.K. Kirby, R.E. Taylor, and P.D. Desai, eds., IFI/Plenum, New York, NY, 1975, vol. 12, p. 400.